Contents lists available at ScienceDirect

CIRP Journal of Manufacturing Science and Technology

Surface location error in robotic milling: Effect of combined low frequency and high frequency vibration modes

Richard Swan [a], Joshua Penney [a], Gregory Corson [a], Jose Nazario [a], Tony Schmitz [a,b,*]

[a] University of Tennessee, Knoxville, Knoxville, TN, USA [b] Oak Ridge National Laboratory, Manufacturing Demonstration Facility, Knoxville, TN, USA

ARTICLE INFO

ABSTRACT

This paper describes surface location error (SLE) for serial kinematic robot milling. It includes frequency-domain models for milling stability and SLE, which both use a mechanistic force model and tool tip frequency response functions as inputs. Based on the predictions, experimental conditions are selected and SLE experiments are completed for a selected geometry and 6061-T6 aluminum workpieces. Measurements and predictions are compared and the predictions are used to compensate the workpiece geometry and reduce SLE. It is observed that, due to the presence of both low stiffness, low frequency robot modes and high frequency tool-holder-spindle modes, the SLE is large, but nearly independent of spindle speed for the available range of spindle speeds.

1. Introduction

Serial kinematic robotic milling offers advantages including high work volume-to-floor space ratio, reconfigurability, and lower cost relative to traditional stacked axis machine tools for the same work volume. However, the pose-dependent, low stiffness and low frequency robot modes can limit part accuracy, surface finish, and material removal rates relative to machine tools. Prior research efforts have studied the relationships between robotic milling configurations, structural dynamics, machining parameters, path planning, and milling performance. Key contributions are summarized and the research objective for this study are provided in the following sections.

1.1. Robotic milling dynamics

As noted, robots are generally less stiff than traditional machine tools and,

frequency response function (FRF), rather than the lower frequency structural modes. Pan et al. [5] reported poor surface finish and Zaghbani et al. [6] applied spindle speed variation to mitigate the effects of these low frequency modes for serial kinematic robots. Maurotto and Tunc [7] showed that chatter, or self-excited vibration, originating from low frequency robot modes can diminish surface integrity. Tunc and Shaw [8,9] measured low frequency modes for parallel kinematic robots and noted their negative influence on milling performance. Schneider et al. [10] proposed that the low frequency robot modes (10 Hz to 20 Hz) result in mode coupling chatter during robotic milling. Additionally, the pose dependence of these low frequency modes complicates robotic milling parameter selection. Tunc et al. [11] and Cen et al. [12] noted that variation in tool tip FRFs results in sensitivity to milling direction. Specifically, the chatter stability limit can depend on the feed direction for robotic milling and this must be considered when selecting stable combinations of spindle speed and depth of cut for arbitrary tool paths.

---

further, the end effector stiffness varies with the robot pose throughout its work volume. Pan et al. [1] reported this reduced stiffness and pose dependence stating that the static stiffness of industrial robots can be significantly lower than traditional machine tools. Abele et al. [2] recognized the pose dependence and commented on its influence on robotic milling force frequency content. Mejri et al. [3] and Mousavi et al. [4] also noted the change in tool tip natural frequencies with robot configuration.

Several researchers have reported that robots are not only less stiff than machine tools, but also that the low stiffness of low frequency modes can adversely affect milling performance. This behavior is different than machine tools, where the tool-holder-spindle flexibility typically dominates the tool tip

Given these challenges, multiple research groups have described modeling strategies to predict and accommodate the low frequency, pose-dependent and high frequency, pose-independent dynamics. Bondarenko et al. [13] simulated tool tip displacements due to dynamic milling forces considering the robot tool tip FRFs. Their study did not consider the effect of robot dynamics on the milling forces, however. Cen and Melkote [14] included the influence of the robot dynamics on milling force and demonstrated that the resulting forces are larger than predictions which do not consider the tool tip FRFs. In related work, Cen and Melkote [15] presented a stiffness model based on the conservative congruence transformation (CCT) that recognized the influence of the milling force on the robot stiffness. Riviere-Lorph`evre `et al. [16] modeled

the robotic milling force considering the axis tilt which is typically present during five-axis tool paths. Cordes et al. [17] considered the influence of low and high frequency modes on robotic milling stability. They noted that the low frequency modes affect low spindle speed milling stability for hard to machine materials, such as titanium alloys, while high frequency modes due to tool-holder-spindle dynamics dominate the stability behavior for higher speed aluminum milling. They provided stability maps for robotic milling in aluminum. Schnoes and Zaeh [18] modeled the mean milling force to identify the optimal workpiece location to minimize tool path deviations.

Many authors have also studied the kinematic redundancy made available when using a six degree of freedom robot to perform five (or less) degree of freedom milling operations. This functional redundancy can be leveraged to modify pose for the same tool tip location in the robotic milling work volume and, subsequently, change the tool tip FRF due to its pose dependence. Lin et al. [19] optimized the spindle configuration based on robot pose, where they mapped the spindle configuration to deformations at the robot end effector. Chen et al. [20] also recognized the tool tip FRF dependence on robot pose. They measured the tool tip FRF for a given tool tip location using multiple robot configurations by leveraging the redundant degree(s) of freedom. Given the measured FRFs, they implemented the inverse distance weighted (IDW) model to interpolate tool tip FRFs for other postures and, using the predicted FRFs, calculated the corresponding stability maps.

Celikag et al. [21] used the redundant degree(s) of freedom to develop a compliance map for the robot work volume at the machining table surface. It was proposed that the map could then be used for static deflection compensation during robotic milling. This effort followed the work of Mousavi et al. [22], who studied the effect of one and two degrees of redundancy on the milling stability limit. Gonul et al. [23] measured the tool tip FRFs and used the kinematic redundancy to reduce the sensitivity of robotic milling stability to work volume location and feed direction. Celikag et al. [24] extended the redundancy concept by continuously varying the robot configuration around its redundancy during milling tool paths. This produced time varying FRFs that served to reduce chatter during robotic milling by disturbing the surface regeneration mechanism responsible for the self-excited vibration. Xiong et al. [25] leveraged the redundant degree(s) of freedom to determine poses for maximized stiffness. They proposed a posture optimization problem that considered joint limits, singularity avoidance, and trajectory smoothness. *1.2. Robotic milling surface location error*

Surface location error (SLE) has been studied extensively to understand and predict part geometry errors caused by the forced vibration response to periodic cutting forces under stable milling conditions. An overview is provided by Schmitz and Smith [26]. While earlier efforts focused on traditional machine tools, more recent research has addressed robotic milling. Corral et al. [27] described a static analysis to calculate surface location error (SLE) maps for discrete points in the robot work volume that considered the position-dependent static stiffness of a parallel kinematic robot. Cen et al. [28] presented the combination of a wireless force sensor and mechanistic force model to improve part accuracy in robotic milling. The compensation was based on the mean force. Hou et al. [29] selected the optimal robot pose for minimum SLE considering the pose-dependent FRFs. This effort was an application of the IDW model [20].

1.3. Research objective

To build on prior robotic milling efforts [30], the objective of this research was to model and compensate SLE for robotic milling of aluminum alloys. Due to the presence of both low stiffness, low frequency robot modes and high frequency tool-holder-spindle modes, it is demonstrated that the SLE is large, but nearly independent of spindle speed for the traditional range of aluminum cutting speeds. This is unlike typical SLE studies, where large variations in workpiece accuracy are observed when the tooth passing frequency is near a system natural frequency (or its first few subharmonics). SLE prediction, measurement, and compensation results are provided to confirm the feasibility of the modeling approach for robotic milling.

The paper is organized as follows. First, the milling stability, SLE, and SLE compensation models are described. Second, the experimental setup details are provided. Third, results are presented for the cutting force model, tool tip FRFs, stability and SLE predictions, SLE measurements, including a comparison to results from a traditional three-axis machine tool, and SLE compensation. Fourth, concluding remarks are provided.

2. Frequency domain process modeling

In this study, the mechanistic cutting force model, which relates the cutting force to chip area, the tool tip FRFs, which include both the pose-dependent robot vibration modes and the pose-independent tool-holder-spindle vibrations modes, and the workpiece FRFs were used as inputs to frequency domain predictions for robotic milling stability and SLE. These predictions enabled informed parameter selection and, ultimately, SLE compensation for improved performance. The predictive algorithms are described in the following paragraphs.

2.1. Stability maps

Altintas and Budak [31] transformed the time-delay dynamic milling equations into a time-invariant, radial immersion-dependent system. They presented a frequency domain solution for the spindle speed-dependent limiting axial depth of cut where they expanded the time-varying coefficients of the milling equations, which depend on the angular orientation of the tool as it rotates through the cut, into a Fourier series and then truncated the series to include only the mean component. They expressed the stability boundary using the eigenvalue problem shown in Eq. (1), where [I] is the 2 × 2 identify matrix, Λ are the two frequency-dependent eigenvalues, and FRF_{or} is the oriented FRF, which depends on the x (feed) and y direction FRFs and directional orientation factors. These factors are defined using the cutting force model and the cut start and exit angles, which depend on the radial depth and milling type (up or down).

$$\det([I]+\Lambda[FRF_{or}]) = 0 \tag{1}$$

Given the two eigenvalues, the limiting axial depth of cut, b_{lim}, for each is defined using Eq. (2), where N_t is the number of teeth on the cutter, k_t is the tangential direction cutting force coefficient, Λ_{Re} is the real part of the complex-valued eigenvalue, and κ is defined in Eq. (3), where ω_c is the chatter frequency should it occur (in rad/s) and τ (in s) is the tooth period. The spindle speed, Ω (in rpm), is calculated using Eq. (4). The minimum b_{lim} value at each spindle speed is selected to define the final stability limit. Additional details and example computer code are provided in Ref. [26].

$$b_{lim} = -\frac{2\pi}{N_t k_t}\left(\frac{\Lambda_{Re}}{1+\kappa^2}\right) \tag{2}$$

$$\kappa = \frac{\Lambda_{Im}}{\Lambda_{Re}} = \frac{\sin\omega_c\tau}{1 - \cos\omega_c\tau} \tag{3}$$

Table 1
Example results for iterative SLE compensation algorithm.

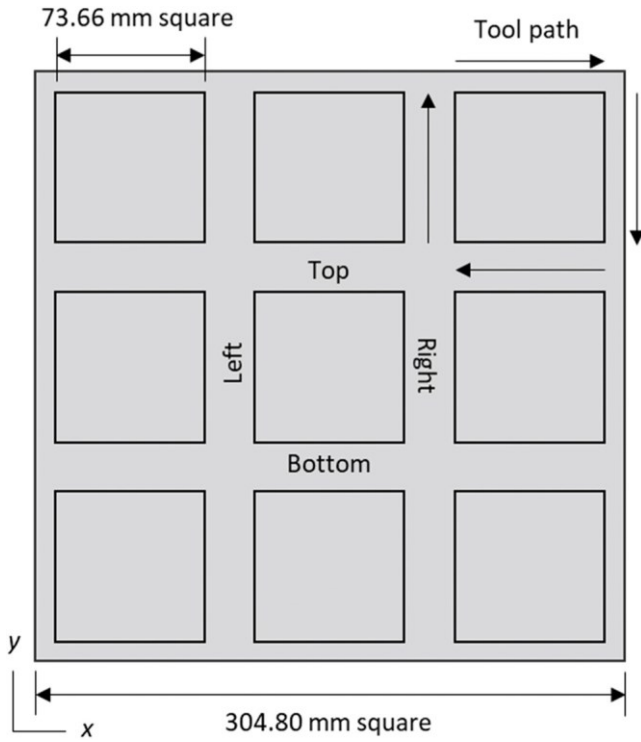| Iteration number	Radial depth (mm)	SLE prediction (μm)	Part error (μm)
1	2.000	184.9	184.9
2	2.185	205.2	20.3
3	2.205	207.7	2.5
4	2.208	207.9	0.2

Fig. 1. SLE workpiece geometry (6061-T6 aluminum). The nominally identical squares were each machined using different conditions during SLE testing to compare the dimensions to SLE predictions.

Fig. 2. Experimental setup showing KUKA KR250 robot, PushCorp STC1515 spindle, KUKA KP2-HV500 rotary positioner, and KUKA KL 4000 linear track.

$$\Omega = \frac{60}{N_t \tau} \tag{4}$$

2.2. SLE maps

Schmitz and Mann [32] described a frequency domain solution for SLE to complement the frequency domain stability solution [31]. To determine SLE, they made two assertions. First, although cutter-workpiece vibrations occur in both the x and y directions, they assumed that the y direction vibrations dominate the final surface location for an x direction feed. Second, they assumed that regeneration can be neglected in stable machining. Based on these assumptions, their concept was to: 1) express the y direction cutting force in the frequency domain, $F_y(\omega)$, using a Fourier series; 2) determine the frequency domain y displacement, $Y(\omega)$, by multiplying $F_y(\omega)$ by the y direction FRF; 3) use the inverse Fourier transform, *ift*, to convert this result to the time domain, $y(t)$, (see Eq. 5); and 4) sample $y(t)$ at the cut entry (up milling) or exit (down milling) to find the SLE.

$$F_y(\omega)\frac{Y}{F_y}(\omega) = Y(\omega) \Rightarrow_{ift} y(t) \tag{5}$$

The y direction cutting force can be described as the Eq. (6) Fourier series using n terms and A axial slices (with index j). The summation over the number of teeth with index i in Eq. (6) incorporates the potential for more than one tooth to be engaged in the cut at any instant
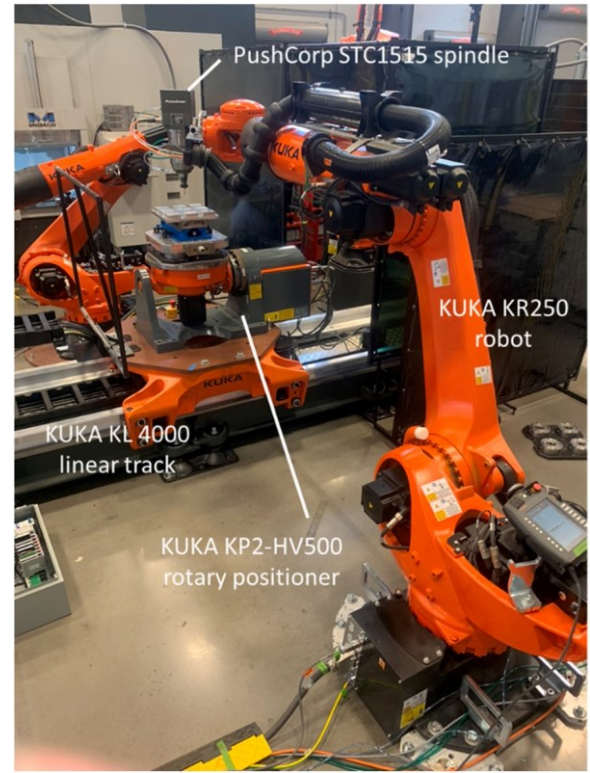
and ϕ_i is the cutter rotation angle for each tooth as defined in Eq. (7). In Eq. (7), ω is the spindle speed (in rad/s) and χ is the rotation angle per axial slice. This rotation angle is defined in Eq. (8), which includes the helix angle, γ, cutter diameter, d, and axial depth per slice, db. The total axial depth of cut, b, is the product Adb. Additional details and example computer code are provided in [26]. The mechanistic force model applied in this research is described in Eqs. (9) and (10).

$$\sum_{j=1}^{A}\sum_{i=1}^{N_t} F_y(\phi) = a_0 + \sum_{n=1}^{\infty}\left(a_n\cos n\phi_i + b_n\sin n\phi_i\right) \tag{6}$$

$$\phi_i = \omega t + \frac{2\pi}{N_t}(i-1) - \chi(j-1) \tag{7}$$

$$\chi = \frac{2db\tan\gamma}{d} \tag{8}$$

2.3. SLE compensation algorithm

The modeled SLE was used to adjust the commanded radial depth of cut and compensate the part geometry error caused by forced vibrations. Because the FRFs in the x and y directions were not necessarily the same, the compensation was completed independently for the two feed directions.

The first step in the compensation algorithm was to select the cutting conditions, including radial depth, feed per tooth, axial depth, spindle speed, and feed direction. The SLE and, therefore, the part error was then predicted. The predicted error was added to the initial radial depth of cut with all other cutting parameters held constant to calculate a new radial depth. Because the radial depth was increased, the SLE also increased. Therefore, the second step was to recalculate the SLE and part error for the new radial depth with all other cutting conditions held constant. The new SLE was again added to the initial

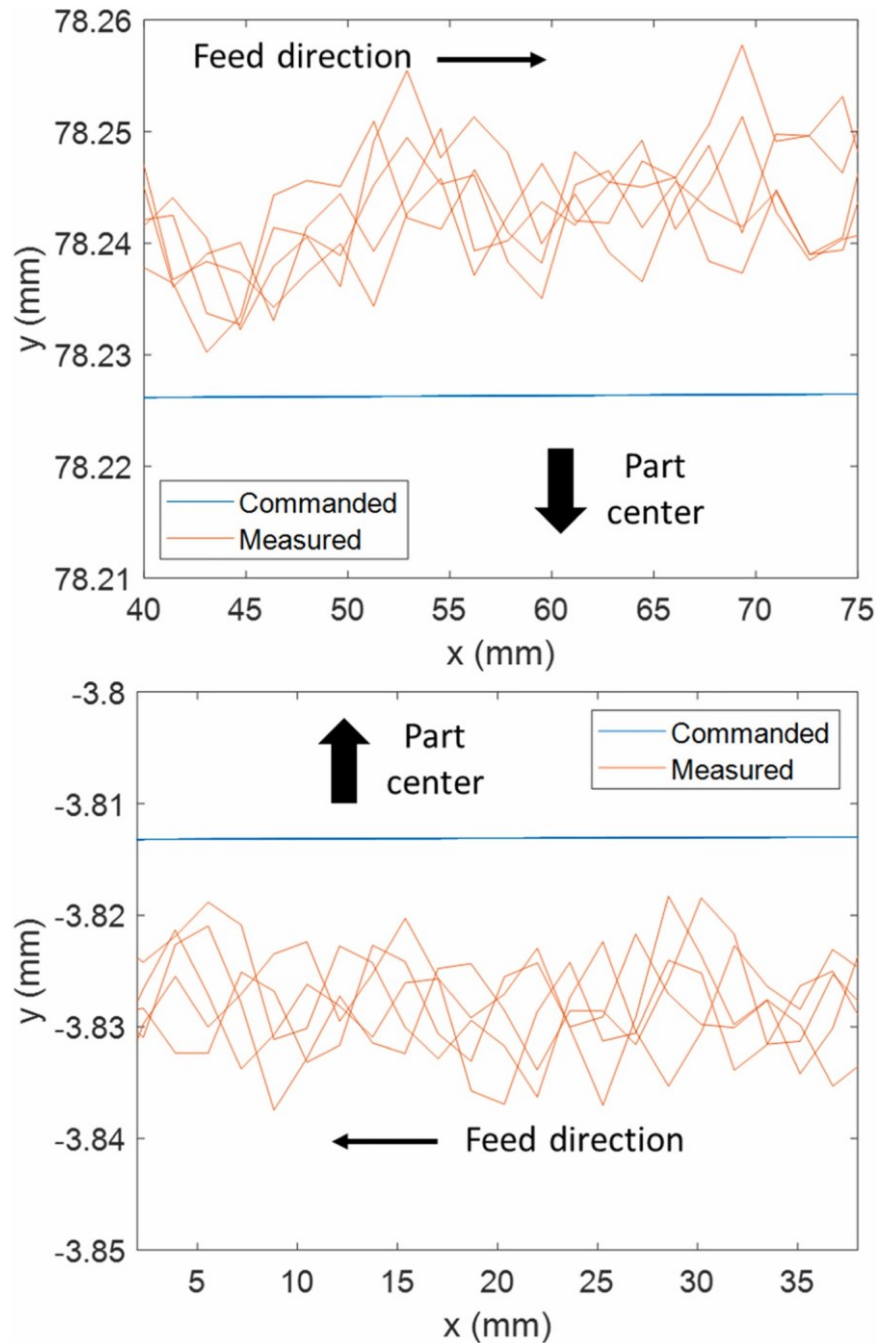radial depth of cut. The iterative process continued until the part error was less than 2 μm.

Fig. 3. Robot end effector path errors for: (top panel) square tool path top (+ *x* direction feed); and (bottom panel) square tool path bottom (-*x* direction feed). The square top and bottom surfaces are identified in Fig. 1.

Table 2
Mean robot end effector path errors for square tool path.

Feed direction	Feed per tooth (mm)	Spindle speed (rpm)	Mean offset (mm)
x (top/bottom)	0.125	10,700	0.014
x (top/bottom)	0.250	10,700	0.032
x (top/bottom)	0.125	10,950	0.014
x (top/bottom)	0.250	10,950	0.034
y (left/right)	0.125	10,700	0.016
y (left/right)	0.250	10,700	0.033
y (left/right)	0.125	10,950	0.016
y (left/right)	0.250	10,950	0.033

vided in Table 1, where the SLE predictions increase with commanded radial depth, but the part error decreases because the increased radial depth compensates for the SLE relative to the desired part dimension.

The algorithm converged within a few iterations. An example is pro-vided in Table 1, where the SLE predictions increase with commanded radial depth, but the part error decreases because the increased radial depth compensates for the SLE relative to the desired part dimension. The result from iteration number 4 would be selected for test conditions in this example. The reader may note that the increased radial depth could affect the milling stability for a fixed axial depth and spindle speed. However, because the SLE is generally much smaller than the radial depth, a change in stability is unlikely in typical applications.

3. Experimental setup

The experimental setup included a PushCorp STC1515 milling spindle mounted to the end effector of a KUKA KR250 R2700 six-axis
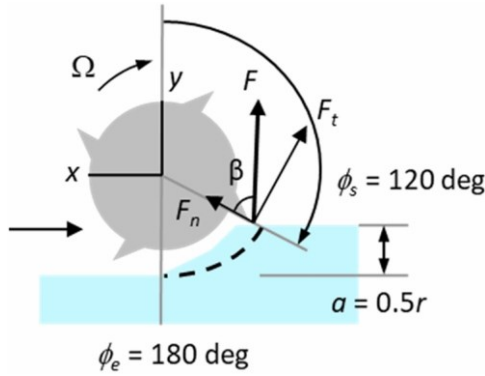
Fig. 4. Down milling geometry and force components for 25% radial immersion.

Table 3
Mechanistic cutting force coefficients.

Coefficient	Value
$k_t\ k_n$	597.3 N/mm^2
	59.8 N/mm^2

industrial robot. The STC1515 spindle had a maximum spindle speed of 15000 rpm, a maximum power of 11.2 kW, and a stall torque of 10 Nm. The KR250 six-axis robot was rated for a payload of up to 250 kg with a manufacturer-specified pose repeatability of ± 0.05 mm. A series of 6061-T6 aluminum workpieces were machined that consisted of nine squares with equal dimensions. The squares were arranged in a grid pattern as shown in Fig. 1; the individual squares were machined using different cutting conditions to compare SLE predictions with measured values.

The Fig. 1 workpieces were mounted to a KUKA KP2-HV500 two-axis rotary positioner using a vise. The rotary positioner had a maximum payload of 500 kg and manufacturer-specified orientation repeatability of ± 0.009°. The rotary

positioner was mounted to a KUKA KL 4000 linear track with a manufacturer-specified positional repeatability of ± 0.02 mm along its single axis. A 12.7 mm diameter, three-flute, 40° helix tool (Accupro 12179740) was mounted in the spindle using a BT30 ER25 collet holder (Kennametal 1258025). The tool extension length from the holder was 42 mm. The spindle-robot-rotary positioner-linear track system is shown in Fig. 2.

The robotic milling tool paths were programmed manually using the KRL programming language. A standard KRL probing cycle was used to identify the workpiece coordinate system before each machining test. This procedure used a spindle-mounted probe to select two points along the square x axis and one point on the square y axis (in the positive y direction); all points were selected at the same z position. This procedure defined the work coordinate system and the tool path for the selected square was executed in this coordinate system.

To provide a comparison to the robotic milling SLE results, the tests were repeated on a Haas VF-4SS three-axis CNC milling machine to determine the SLE for the new dynamic system. The same tool and extension length, as well as the same part geometry and material, were used, although a new ER32 collet holder (Accupro 775656) was selected because the spindle interface was CT40, not BT30. The VF-4SS spindle had a maximum spindle speed of 12,000 rpm, 22.4 kW of power, and a maximum torque of 122 Nm.

Before and after the machining tests on both the robot and conventional machine tool, the workpieces were measured using a Zeiss Duramax coordinate measuring machine (CMM). The CMM measurement uncertainty was specified as 2.5 μm for the temperature range in the test environment (standard manufacturing facility).

4. Results

4.1. Local robot path accuracy

Robot part path accuracy is generally inferior to traditional machine tools. This is the result of the common pick-and-place activities of robots which require accurate start/end positions, but do not require an accurate trajectory to be followed between the start and end positions. To
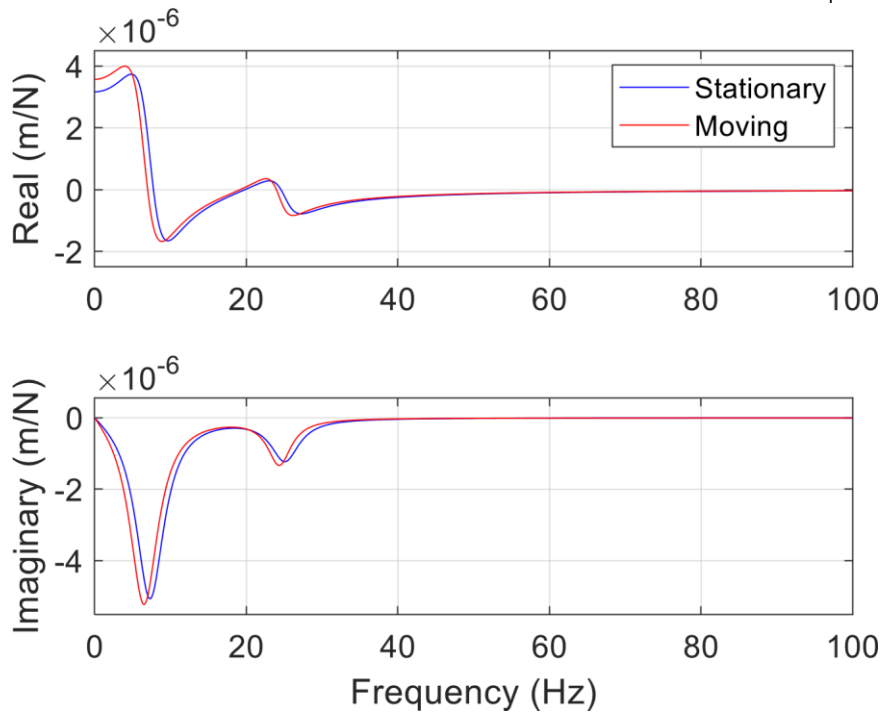

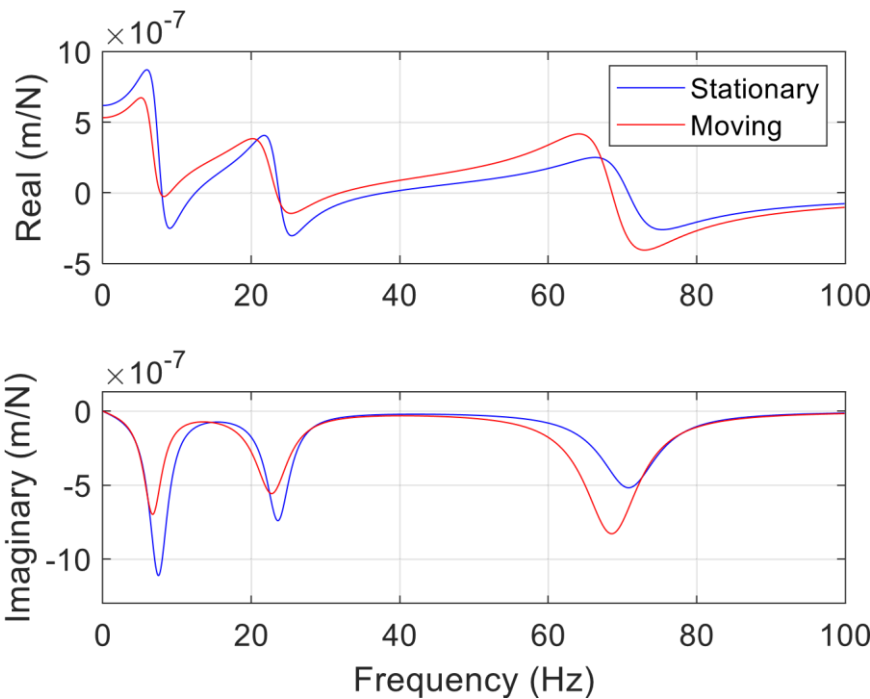**Fig. 5.** Moving and stationary FRFs for spindle-robot in the *x* direction.

Fig. 6. Moving and stationary FRFs for spindle-robot in the *y* direction (note the change in vertical scale relative to Fig. 4).

Table 4
Modal parameters for the spindle-robot tool tip FRFs in the *x* and *y* directions.

Mode	x direction			y direction		
	Natural frequency (Hz)	Modal stiffness (N/m)	Modal damping ratio (-)	Natural frequency (Hz)	Modal stiffness (N/m)	Modal damping ratio (-)
1	8.4	594,131	0.182	7.8	735,3812	0.195
2	26.1	4,025,191	0.091	24.4	4,095,314	0.090
3	63.3	6,270,000	0.086	69.5	9,240,824	0.087
4	71.3	14,700,000	0.040	85.0	33,800,000	0.081
5	123.0	38,300,000	0.074	122.0	11,000,000	0.090
6	176.5	97,100,000	0.072	220.7	13,200,000	0.132
7	200.8	27,200,000	0.172	676.5	14,500,000	0.185
8	272.5	72,600,000	0.049	1184.0	23,000,000	0.228
9	287.5	222,000,000	0.014	1480.0	64,700,000	0.048
10	657.8	12,300,000	0.152	2197.0	599,000,000	0.025
11	1014.5	63,600,000	0.175	2404.0	223,000,000	0.013
12	1443.5	33,000,000	0.069	2672.0	518,000,000	0.031
13	2223.8	110,000,000	0.060	2933.3	58,900,000	0.079
14	2439.3	148,000,000	0.022	4362.3	62,800,000	0.210
15	2786.5	280,000,000	0.032	5257.8	133,000,000	0.024
16	3114.3	56,300,000	0.096	5418.8	27,600,000	0.011
17	4519.5	68,700,000	0.115	6622.8	903,000,000	0.008
18	5311.3	101,000,000	0.022			
19	5434.3	28,800,000	0.011			
20	6629.3	910,000,000	0.008			

evaluate the robot path accuracy local to the workpiece, it was programmed to follow the square path used to machine the squares shown in Fig. 1. The square tool path was approximately 74 mm per side and was repeated five times with a step down in the z direction (i.e., toward the part) between each repetition. The end effector positional data was recorded by the robot controller and compared to the commanded positional profile. The results for two opposing sides of the square are displayed in Fig. 3. It is observed that the actual path is located outside the commanded square path (i.e., toward the exterior of the part) in both cases. The offsets would result in less material being removed than commanded (i.e., an undercut surface) when machining a square using this tool path. It was determined that the oscillatory motion observed in these plots occurred at a low frequency mode of the robot. Comparisons to a

separate setup, where a capacitance probe was mounted in the spindle and used to measure robot motions against a calibrated artifact, confirmed the validity of the robot controller data for the local work volume defined by the workpiece. [The reader may also note that the robot manufacturer offers on-site calibration, but it was not used for this study.].

The mean offset was determined for the *x* and *y* feed directions at all four feed rates used for SLE testing (feed per tooth values of 0.125 mm and 0.250 mm; spindle speeds of 10700 rpm and 10,950 rpm). The results are shown in Table 2. While these values are small relative to the commanded radial depth of cut (2 mm), they are relevant to the SLE predictions and therefore included in the analysis.

Fig. 7. Setup for workpiece mounted in a vise attached to the top axis (rotation about z axis) of the rotary positioner. The x and y machining directions are identified and the tool-holder-spindle attached to the robot end effector is shown.

r, where the feed direction is x. The two force components are defined in Eqs.

Mode	Natural frequency (Hz)	Modal stiffness (N/ m)	Modal damping ratio (dimensionless)	Natural frequency (Hz)	Modal stiffness (N/ m)	Modal damping ratio (dimensionless)
1	171	127,262,000	0.082	750	720,143,000	0.041
2	472	153,488,000	0.073	1005	134,598,000	0.041
3	954	108,644,000	0.089	1265	71,465,500	0.092
4	1405	56,566,900	0.048	1517	183,073,000	0.050
5	2153	365,370,000	0.079	1702	584,354,000	0.022
6	2803	716,981,000	0.056	2126	336,327,000	0.074
7	3470	107,725,000	0.048	3483	115,208,000	0.058
8	4237	120,550,000	0.049	4224	115,607,000	0.043
9	4847	26,942,100	0.046	4848	31,151,700	0.040
10	5710	45,192,000	0.061	5715	48,556,500	0.064

4.2. Force model coefficients

A mechanistic force model was implemented to relate the machining parameters to the cutting force components in the tangential, F_t, and normal, F_n, directions. Fig. 4 displays the geometry for a 25% radial

Table 5

immersion down milling cut with spindle speed Ω. The start angle, ϕ_s, and exit angle, ϕ_e, are shown for a radial depth of cut, a, equal to half the cutter radius,

(9) and (10), where f_t is the feed per tooth, b is the axial depth of cut, the instantaneous chip thickness is $h = f_t \sin\phi$, and the coefficient subscripts denote the tangential t and normal n directions. The rotating coordinate system forces were projected into the x and y directions using the time-dependent cutter angle, ϕ, to determine the fixed coordinate system time-dependent force components used for SLE predictions.

$$F_t = k_t b h = k_t b f_t \sin\phi \tag{9}$$

$$F_n = k_n b h = k_n b f_t \sin\phi \tag{10}$$

The resultant cutting force, F, is also displayed in Fig. 4. This force is the vector combination of F_t and F_n as shown in Eq. 11. It is oriented relative to the surface normal direction by the force angle, β. The rotating coordinate system resultant force can also be projected into the fixed coordinate system x and y directions using β and ϕ.

$$F = \left(F_t^2 + F_n^2 \right)^{0.5} \tag{11}$$

The cutting force coefficients were determined by measuring the cutting force in the x (feed) and y directions for known machining parameters using a Kistler 9257B dynamometer. The down milling conditions were a = 2 mm, b = 2 mm, and Ω = 10700 rpm. The feed per tooth values were {0.100, 0.150, 0.200, 0.250, and 0.300} mm. A linear regression was applied to the mean force values in the x and y directions over the five feed per tooth values. The slope and intercept values from the linear regressions for the two directions were used to calculate the coefficients [26]; see Table 3.

4.3. Structural dynamics

As reported by Mohammadi and Ahmadi [33], the robotic tool tip FRFs can exhibit nonlinear behavior. This was observed as a dependence of the FRFs and corresponding modal parameters on the harmonic force input level. For this testing, the expected cutting force level was calculated using Eqs. (9)–(11) and the coefficients from Table 3 for the range

Modal parameters for the workpiece-rotary positioner-linear track FRFs in the x and y directions.

	x direction			y direction		
Mode	Natural frequency (Hz)	Modal stiffness (N/ m)	Modal damping ratio (dimensionless)	Natural frequency (Hz)	Modal stiffness (N/ m)	Modal damping ratio (dimensionless)
1	14.5	29,656,352	0.105	14.5	6,249,330	0.105
2	35.1	13,908,773	0.098	25.2	1,7070,058	0.091
3	57.2	31,307,647	0.073	35.9	56,790,910	0.043
4	80.9	47,923,792	0.066	48.1	10,558,127	0.056
5	102.2	68,406,951	0.045			

Table 6
Modal parameters for the Haas VF-4SS tool tip FRFs i   n the x and y directions.

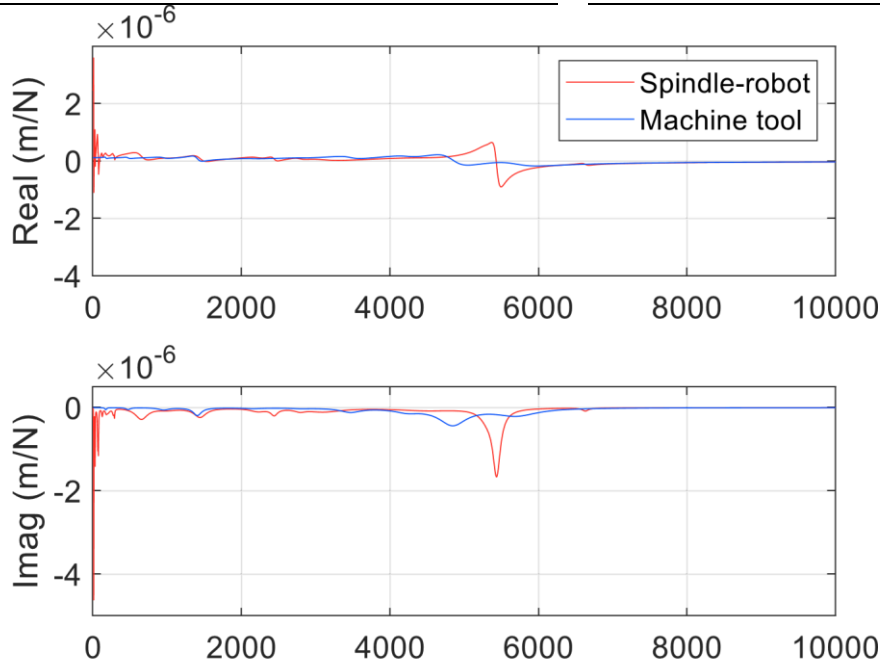*x* direction   *y* direction

Fig. 8. Tool tip FRFs for the spindle-robot and machine tool in the *x* direction.
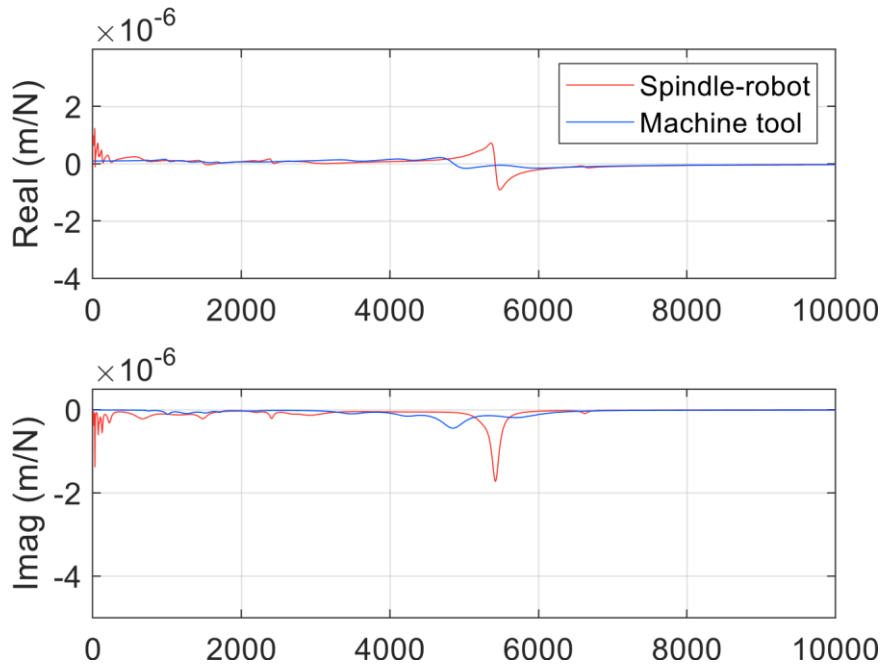

Fig. 9. Tool tip FRFs for the spindle-robot and machine tool in the *y* direction.

of parameters used in the SLE testing. For a 2 mm radial depth, the predicted resultant cutting force was between 82 N (b = 1.5 mm and f_t = 0.125 mm) and 273 N (b = 2.5 mm and f_t = 0.250 mm). The tap testing force level was 125 N to 250 N. Given the overlapping force levels, the measured FRFs were assumed to represent the dynamic behavior during milling.

As shown by Tunc and Gonul [34], robot dynamics can differ depending on whether the robot is moving or stationary when measuring the tool tip FRF. The tool tip FRFs were therefore measured under both stationary and moving conditions (2 mm/s constant velocity motion). The tap testing was completed using an instrumented hammer (PCB 086C04) and low mass accelerometer (PCB 352C23). Assessment of the FRF coherence and comparison to laser vibrometer measurements confirmed the reliability of the accelerometer-

based FRF measurements. It was observed that the low frequency robot modes were modified when the robot was in motion; see Fig. 5 for the *x* direction and Fig. 6 for the *y* direction. The modes associated with the tool-holder-spindle were not affected, as anticipated. The modal parameters for the spindle-robot in the *x* and *y* directions are provided in Table 4, where the low frequency robot modes are based on the moving FRF results. Additionally, the tool tip FRFs were measured at the workpiece corner locations (see Fig. 1 for workpiece geometry) with the workpiece mounted on the rotary positioner. The FRFs did vary with robot pose, as reported by other authors. Therefore, the rotary positioner-linear track was used to move each
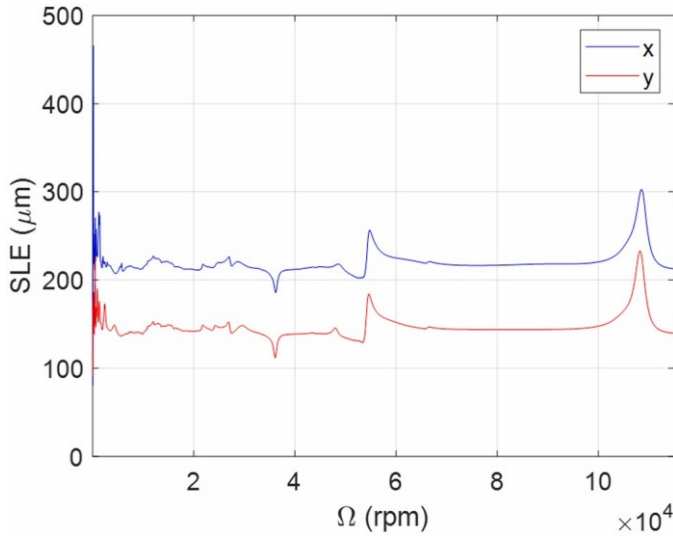
Fig. 10. Predicted spindle-robot SLE map for *x* and *y* part dimensions (2.5 mm axial depth and 0.250 mm feed per tooth).
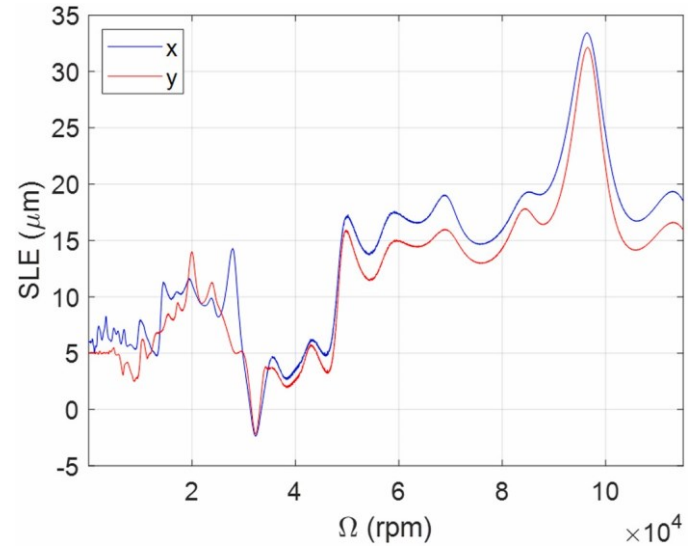
Table 7

Machining parameters for SLE testing.

square to a fixed location relative to the robot when completing the machining tests. This was accomplished by collocating the workpiece center with the center of rotation for the top rotary axis, which rotated about the *z* axis, and
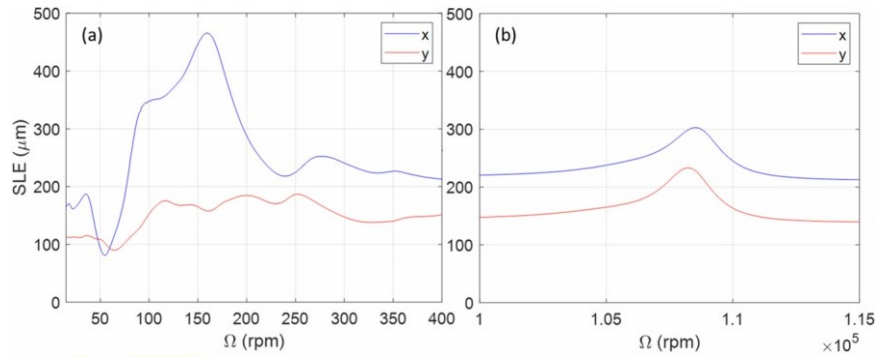

Fig. 11. (a) Predicted SLE at low spindle speeds due to the low frequency (8.4 Hz in *x* direction) spindle-robot modes; and (b) predicted SLE at high spindle speeds due to the high frequency (5418.4 Hz in *y* direction) tool-holder-spindle modes. The parameters are 2.5 mm axial depth and 0.250 mm feed per tooth as in Fig. 10.
Note that the mean value of the high spindle speed SLE is increased due to the low frequency, low stiffness spindle-robot modes.

using a combination of *z* axis rotations and *x* axis translations to position each square at a common location for the machining tests.

The workpiece FRFs were also measured to incorporate the workpiece-rotary positioner-linear track dynamics in the SLE predictions; the workpiece setup is displayed in Fig. 7. The associated modal parameters are given in Table 5 for the two directions. The most flexible mode was observed in the *y* direction at a natural frequency of 14.5 Hz. This is due to rotation about the *x* axis for the bottom rotary axis. The force applied at the workpiece in the *y* direction produced a moment about the *x* axis which excited the low frequency 14.5 Hz mode. The same mode is observed in the *x* direction, but with 4.75 times higher stiffness, due to measurement cross talk (i.e., the force input direction and accelerometer axis were not perfectly aligned with the rotary positioner-linear track axes). The stability and SLE predictions were completed using the sum of the spindle-robot and rotary positioner- linear track FRFs for both the *x* and *y* directions.

Because comparison SLE tests were completed using a traditional three-axis CNC machine tool with the same endmill and workpiece, the tool tip FRFs for the machine tool were also measured and modal fitting was performed. For the machine tool, the axes were stationary; no change in FRFs with machine motion or tool tip location within the work

Test condition	Radial depth (mm)	Axial depth (mm)	Feed per tooth (mm)	Spindle speed (rpm)
1	2	1.5	0.125	10,700
2	2	1.5	0.250	10,700
3	2	2.5	0.125	10,700
4	2	2.5	0.250	10,700
5	2	1.5	0.125	10,950
6	2	1.5	0.250	10,950
7	2	2.5	0.125	10,950
8	2	2.5	0.250	10,950

volume was assumed. The *x* and *y* direction modal parameters are listed in Table 6. Comparisons between the tool tip FRFs for the spindle-robot and CNC machine tool are displayed in Fig. 8 (*x* direction) and Fig. 9 (*y* direction). The scaling for both plots is identical. The large vertical axis ranges are set by the 8.4 Hz *x* direction robot mode previously shown in Fig. 5 (*x* direction mode 1 from Table 4). Two key attributes of Figs. 8 and 9 are: 1) the low frequency modes are much more flexible for the spindle-robot; and 2) the tool-holder bending mode is similar for the two setups, but there is an interaction with a spindle mode on the machine tool that produces two adjacent modes with increased dynamic stiffness. This is caused by the dynamic absorber effect previously reported by

Fig. 12. Predicted machine tool SLE map for *x* and *y* square dimensional errors (2.5 mm axial depth and 0.250 mm feed per tooth). Note the order of magnitude change in vertical scale relative to Fig. 10.

Table 8

SLE predictions and measurements for spindle-robot and machine tool.

	Spindle-robot	Machine tool

Test condition	Predicted SLE (μm)		Measured SLE (μm)		Predicted SLE (μm)		Measured SLE (μm)	
	X	y	x	y	x	y	x	y
1	69	48	30	81	1.5	1.1	-8.6	-5.9
2	141	97	130	133	3.0	2.1	-4.8	-5
3	106	71	97	116	3.7	3.0	-4.5	-3.9
4	216	143	211	166	7.4	6.0	-0.4	0.9
5	69	48	31	78	1.4	0.9	-9.3	-7.4
6	144	99	138	131	2.8	1.9	-4.6	-4.9
7	108	73	96	110	3.5	2.7	-4.6	-4.5
8	222	147	222	168	6.9	5.4	1.1	0.7

Duncan et al. [35], which occurs when a tool-holder bending mode natural frequency is near one or more spindle mode natural frequency (s).

4.4. Stability predictions

Stability maps were calculated using the frequency domain mean force algorithm [31], modal parameters from Tables 4–6, cutting force coefficients from Tables 3, and 2 mm radial depth down milling. Four maps were calculated using the x and y feed directions for the spindle-robot and machine tool. The minimum critical stability limit was obtained for the spindle-robot x direction feed. Based on this critical stability limit, two stable axial depths were selected for testing: 1.5 mm and 2.5 mm. The maximum spindle speed for testing was defined by the Haas VF-4SS. The reader may note that this stability analysis was based only on regenerative chatter only; mode coupling was not considered.

4.5. SLE predictions

SLE maps were calculated using the frequency domain SLE algorithm [32], modal parameters from Tables 4–6, cutting force coefficients from Table 3, and a 2 mm radial immersion for down milling. SLE maps were calculated for combinations of: 1) the x and y direction square dimensions for the spindle-robot and machine tool; 2) axial depths of 1.5 mm and 2.5 mm; and 3) feed per

tooth values of 0.125 mm and 0.250 mm. Note that the x direction part dimensions (i.e., the left and right surfaces of the square) were calculated using the x direction FRFs because this is the surface normal direction. Similarly, the y direction part dimensions (i.e., top and bottom surfaces of the square) were calculated using the y direction FRFs.

The spindle-robot SLE map for the x and y square dimensional errors is displayed in Fig. 11, where the axial depth is 2.5 mm and the feed per tooth is 0.250 mm. In this map, a positive SLE value indicates an undercut condition, where less material than commanded was removed. To demonstrate the combined effect of the low frequency robot modes and the high frequency tool-holder-spindle modes, a spindle speed range of 15 rpm to 115,000 rpm was selected. This wide range was set by the spindle-robot most flexible modes at 8.4 Hz (x direction) and 7.8 Hz (y direction); see Table 4 and Figs. 8 and 9. Note that Fig. 10 also includes the offset due to robot positioning error identified in Table 2 for the 0.250 mm feed per tooth value. The large vertical scale in Fig. 10 is set by the large SLE variation that corresponds to the 8.4 Hz x direction robot mode.

For the 8.4 Hz robot mode, the spindle speed that matches the tooth passing frequency to this natural frequency is $\Omega = \frac{8.4(60)}{3} = 168$ rpm. The largest variation in SLE due to the low frequency mode occurs near this low spindle speed; see Fig. 11(a). At spindle speeds above 168 rpm, the 8.4 Hz mode contributes a large positive SLE value, but no significant SLE variation. For the 5418.4 Hz tool-holder-spindle mode, on the other hand, the spindle speed that matches the tooth passing frequency to this natural frequency is $\Omega = \frac{5418.8(60)}{3} = 108376$ rpm; see Fig. 11(b). The largest variation in SLE due to the high frequency mode occurs near this much higher spindle speed. Other significant SLE variations occur near integer fractions of these natural frequencies. For the 8.4 Hz mode, the next three variations occur at {84, 56, and 42} rpm. For the 5418.8 Hz mode, the next three variations occur at {54188, 36125, and 27094} rpm. For the available spindle speed range (up to 12000 rpm), the combined effect of the low and high frequency modes is large SLE that is nearly independent of spindle speed. This is observed as the nearly horizontal SLE trend near 10,000 rpm.
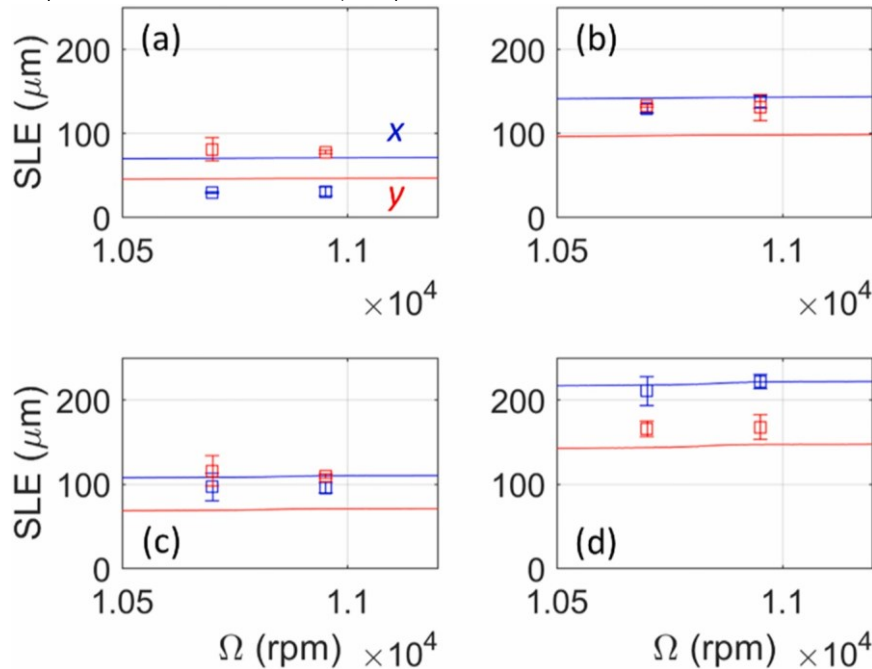

Fig. 13. SLE testing results for spindle-robot. (a) 0.125 mm feed per tooth, 1.5 mm axial depth; (b) 0.250 mm feed per tooth, 1.5 mm axial depth; (c) 0.125 mm feed per tooth, 2.5 mm axial depth; and (d) 0.250 mm feed per tooth, 2.5 mm axial depth.
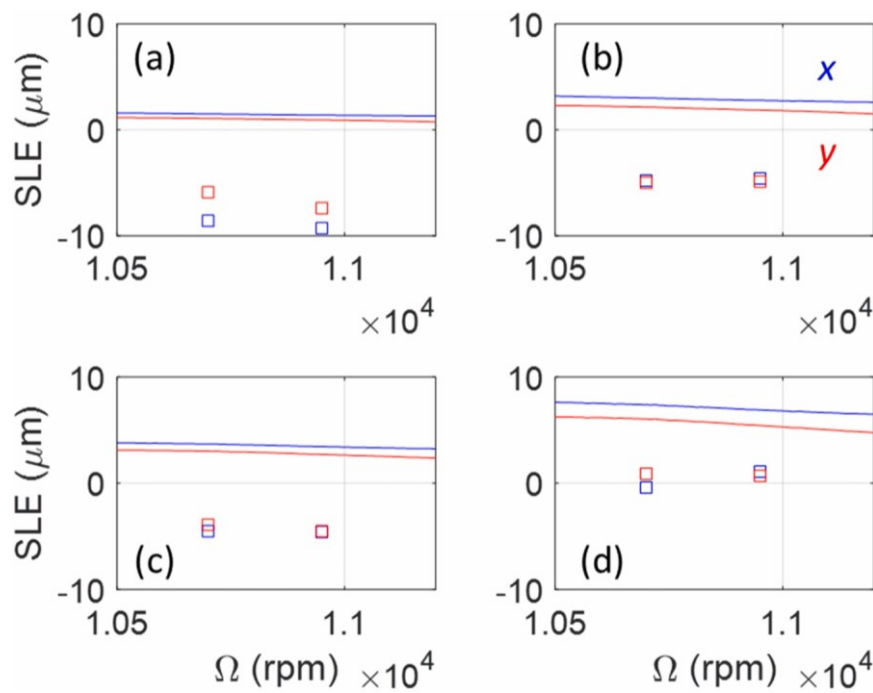
Fig. 14. SLE testing results for machine tool. (a) 0.125 mm feed per tooth, 1.5 mm axial depth; (b) 0.250 mm feed per tooth, 1.5 mm axial depth; (c) 0.125 mm feed per tooth, 2.5 mm axial depth; and (d) 0.250 mm feed per tooth, 2.5 mm axial depth. Note the order of magnitude difference in vertical scales relative to Fig. 12.
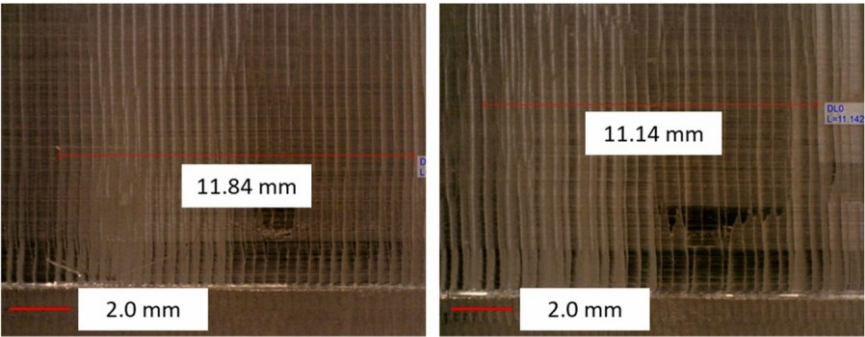

Fig. 15. Machined surfaces from spindle-robot SLE tests for (a) x direction face of square; and (b) y direction face.

The machine tool SLE map for the x and y square dimensional errors is displayed in Fig. 12, where the axial depth is 2.5 mm and the feed per tooth is 0.250 mm to provide a direct comparison to Fig. 10. In this case, the low frequency modes are stiff and the tool-holder-spindle modes dominate the SLE predictions. However, because the most flexible mode has a high natural frequency (4847 Hz, $\Omega = \frac{4847_3(60)}{} = 96940$ rpm), the SLE sensitivity to spindle speed is again low in the allowable spindle speed range (up to 12000 rpm). The x and y direction SLE predictions are similar because the tool tip FRF is essentially symmetric.

Table 9
SLE measurements pre- and post-compensation for spindle-robot.

Test condition	Spindle-robot				
	Measured SLE pre-compensation (μm)			Measured SLE post- compensation (μm)	
	x	y		x	y
1	30	81		-35.5	25.9
2	130	133		-22.4	17.2
3	97	116		-14.4	30.1
4	211	166		1	16.8
5	31	78		-25.8	41.7
6	138	131		-3.3	26.8
7	96	110		4.9	54.1
8	222	168		25.6	28.4

Fig. 16. Machined surface from machine tool SLE tests.
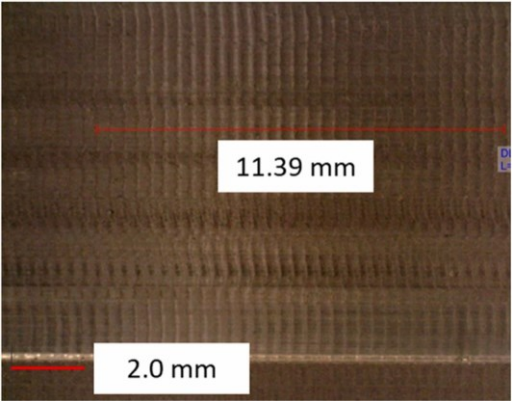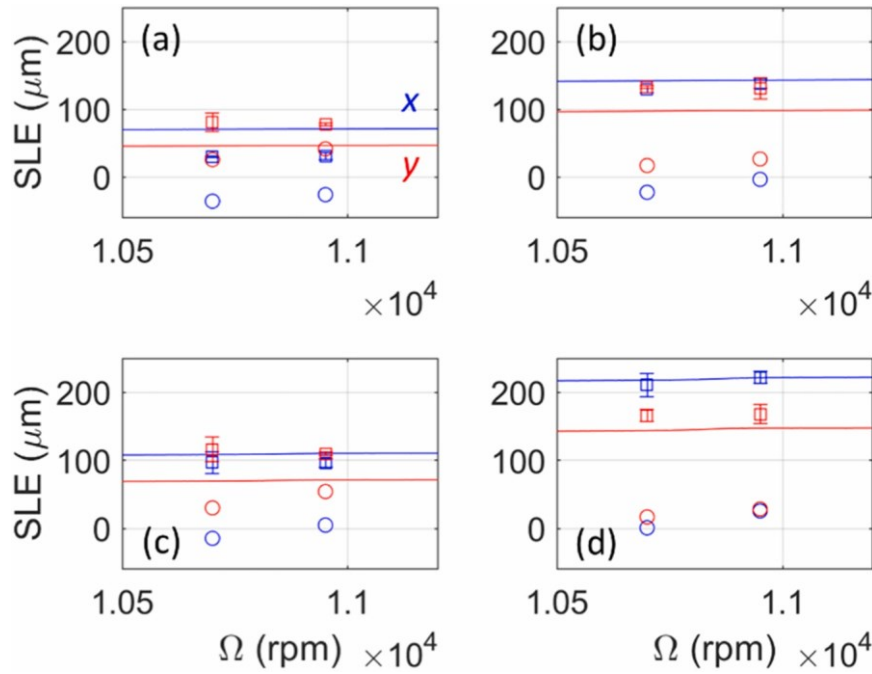
Fig. 17. SLE compensation results for spindle-robot. (a) 0.125 mm feed per tooth, 1.5 mm axial depth; (b) 0.250 mm feed per tooth, 1.5 mm axial depth; (c) 0.125 mm feed per tooth, 2.5 mm axial depth; and (d) 0.250 mm feed per tooth, 2.5 mm axial depth. The squares denote the pre-compensation SLE measurements and the circles denote the post-compensation SLE measurements. A successful outcome is zero values for the circles.

4.6. SLE measurements

Based on the SLE predictions from Fig. 10, SLE tests were performed to machine the eight outer squares from Fig. 1 (the center square served as a reference for the CMM measurements) using eight combinations of machining parameters. These SLE tests were performed using both the spindle-robot and machine tool. The squares were then measured using the CMM to compare the measured and predicted SLE values for the x and y directions. To determine SLE, the differences in the dimensions of each square before and after machining were calculated from the CMM measurement data. The measured radial depth along each surface was taken to be half of the total difference in the square dimensions because the cutting tool removed material around the entire perimeter of the square. The resulting SLE was the difference between the measured radial depth and the commanded radial depth. The endmill diameter was assumed to be correct (12.7 mm). The machining parameters are listed in Table 7. The selected spindle speeds bracket the 10th subharmonic of the 5418.8 Hz tool-holder-spindle mode for the robot spindle, i.e., $\Omega = \frac{5418.8(60)}{3(10)}$

= 10837.6 rpm.

The SLE testing results are provided in Table 8 and Fig. 13 (spindle- robot) and 14 (machine tool), where the figure panels display the four combinations of axial depth and feed per tooth values. The solid lines represent the SLE predictions and the squares identify the measurements. Also, blue lines and squares indicate the x direction results, while red lines and squares indicate the y direction results. The spindle-robot measurements included three repetitions using three nominally identical workpieces to assess repeatability. The reported results for the spindle-robot are the mean values from three measurements of each condition; two-standard deviation (95% confidence interval) error bars are included in Fig. 13 to indicate the process repeatability. The standard deviations from the 16 cases (eight test conditions for two directions) varied between 0.4 µm and 9.0 µm with a mean value of 4.5 µm.

From Figs. 13 and 14, it is observed that: 1) the spindle-robot SLE is much larger than the machine tool; 2) the SLE is nearly independent of spindle speed for the available spindle speed range (up to 12000 rpm); 3) there is some disagreement between the predictions and measurements (e.g., the machine tools results show a 6 µm bias on average, but this is at the limit of the capabilities of the machining and measurement equipment used in this study), but the trends are correct (proportional increases in SLE with increased feed

per tooth or axial depth); and 4) the spindle-robot results are repeatable (standard deviation of three measurements is 4.5 µm, on average). The latter observation provides a pathway for SLE compensation.

4.7. Surface finish

A digital microscope was used to compare the surface finish of the SLE surfaces produced by the spindle-robot and machine tool. Fig. 15 displays the spindle-robot machined surfaces and Fig. 16 shows a machine tool machined surface. The surfaces are similar, although the finish is more uniform for the machine tool as expected. Both the x and y directions are included for the spindle-robot because the low frequency modes were different.

4.8. Robotic milling SLE compensation

The compensation algorithm described previously was implemented using the SLE predictions. The results are shown in Table 9 and Fig. 17, where the lines again identify the SLE predictions, the squares indicate the pre-compensation SLE measurement results, and the circles identify the post-compensation measurement results. The objective was to obtain zero SLE after compensation, so circles near zero SLE indicate a successful outcome. The worst case was overcompensation for test conditions 1 and 5 in the x direction (0.125 mm feed per tooth, 1.5 mm axial depth). This naturally corresponds to the least accurate SLE predictions. The best case was a reduction from 211 µm to 1 µm for test condition 4 in the x direction. In general, the compensation using the predicted SLE values improved the workpiece geometric accuracy.

5. Conclusions

This paper added to prior robotic milling efforts by modeling and compensating SLE for robotic milling of aluminum alloys. It was demonstrated that the SLE was large for robotic milling, but nearly independent of spindle speed within the typical range of cutting speeds for aluminum alloys due to the presence of both low frequency, low stiffness robot modes and higher frequency, higher stiffness tool-holder-spindle modes. SLE prediction, measurement, and compensation results were provided to confirm the feasibility of the modeling approach for robotic milling.

This research provides an initial effort for robotic milling SLE prediction and compensation, but additional studies should follow. These include:

- implementation of the frequency domain stability and SLE models on other robotic milling systems
- measurement of contouring accuracy for robotic milling systems and strategies for improvement, if necessary
- continued evaluation of the difference between robot dynamics when stationary and moving and, by extension, the effect on SLE
- inclusion of the potential for nonlinear robot dynamics (i.e., sensitivity to cutting force level) in the stability and SLE models and quantification of the effect on SLE
- application of the SLE prediction to larger parts, where the tool tip dynamics vary significantly over the required work volume
- SLE prediction and compensation for more complicated part geometries, including those that require five-axis machining
- if accurate stability and SLE predictions are possible, confirm that robotic milling can meet surface finish requirements for machined parts.

CRediT authorship contribution statement

Richard Swan: Conceptualization, Methodology, Software, Validation, Formal analysis, Investigation, Data curation, Writing – draft, Visualization. **Joshua Penney:** Software, Investigation, Writing – Editing, Supervision. **Greg Corson:** Methodology, Software, Validation, Investigation, Data curation. **Jose Nazario:** Conceptualization, Methodology, Investigation, Writing – Editing. **Tony Schmitz:** Conceptualization, Methodology, Software, Validation, Formal analysis, Investigation, Resources, Data curation, Writing – Draft, Writing – Editing, Visualization, Supervision, Project Management, Funding acquisition.

Declaration of Competing Interest

The authors declare that they have no known competing financial interests or personal relationships that could have appeared to influence the work reported in this paper.

References

[1] Pan Z, Zhang H, Zhu Z, Wang J. Chatter analysis of robotic machining process. J Mater Process Technol 2006;173(3):301–9.
[2] Abele E, Weigold M, Rothenbücher S. Modeling and identification of an industrial robot for machining applications. CIRP Ann 2007;56(1):387–90.
[3] Mejri S, Gagnol V, Le TP, Sabourin L, Ray P, Paultre P. Dynamic characterization of machining robot and stability analysis. Int J Adv Manuf Technol 2016;82:351–9.
[4] Mousavi S, Gagnol V, Bouzgarrou BC, Ray P. Dynamic modeling and stability prediction in robotic machining. Int J Adv Manuf Technol 2017;88:3053–65.
[5] Pan Z, Zhang H, Zhu Z, Wang J. Chatter analysis of robotic machining process. J Mater Process Technol 2006;173(3):301–9.
[6] Zaghbani I, Songmene V, Bonev I. An experimental study on the vibration response of a robotic machining system. Proc Inst Mech Eng Part B: J Eng Manuf 2013;227 (6):866–80.
[7] Maurotto A, Tunc LT. Effects of chattering on surface integrity in robotic milling of alloy 690. In: Pressure vessels and piping conference (Vol. 57991, p. V06AT06A004). American Society of Mechanical Engineers; 2017.
[8] Tunc LT, Shaw J. Experimental study on investigation of dynamics of hexapod robot for mobile machining. Int J Adv Manuf Technol 2016;84:817–30.
[9] Tunc LT, Shaw J. Investigation of the effects of Stewart platform-type industrial robot on stability of robotic milling. Int J Adv Manuf Technol 2016;87:189–99.
[10] Schneider U, Drust M, Ansaloni M, Lehmann C, Pellicciari M, Leali F, Gunnink JW, Verl A. Improving robotic machining accuracy through experimental error investigation and modular compensation. Int J Adv Manuf Technol 2016;85:3–15.
[11] Tunc LT, Stoddart D. Tool path pattern and feed direction selection in robotic milling for increased chatter-free material removal rate. Int J Adv Manuf Technol 2017;89:2907–18.
[12] Cen L, Melkote SN, Castle J, Appelman H. A method for mode coupling chatter detection and suppression in robotic milling. J Manuf Sci Eng 2018;140(8):081015.
[13] Bondarenko D, Pashkevich A, Briot S, Ritou M, Furet B. Elasto-dynamic model of robotic milling process considering interaction between tool and workpiece. In: Engineering systems design and analysis (Vol. 44861, pp. 217–226). American Society of Mechanical Engineers; 2012.
[14] Cen L, Melkote SN. Effect of robot dynamics on the machining forces in robotic milling. Procedia Manuf 2017;10:486–96.
[15] Cen L, Melkote SN. CCT-based mode coupling chatter avoidance in robotic milling. J Manuf Process 2017;29:50–61.
[16] Rivì`ere-Lorphevre E, Huynh HN, Ducobu F, Verlinden O. Cutting force prediction` in robotic machining. Procedia CIRP 2019;82:509–14.
[17] Cordes M, Hintze W, Altintas Y. Chatter stability in robotic milling. Robo Comput- Integr Manuf 2019;55:11–8.
[18] Schnoes F, Zaeh MF. Model-based planning of machining operations for industrial robots. Procedia CIRP 2019;82:497–502.
[19] Lin Y, Zhao H, Ding H. Spindle configuration analysis and optimization considering the deformation in robotic machining applications. Robot Comput-Integr Manuf 2018;54:83–95.
[20] Chen C, Peng F, Yan R, Fan Z, Li Y, Wei D. Posture-dependent stability prediction of a milling industrial robot based on inverse distance weighted method. Procedia Manuf 2018;17:993–1000.
[21] Celikag H, Sims ND, Ozturk E. Cartesian stiffness optimization for serial arm robots. Procedia CIRP 2018;77:566–9.
[22] Mousavi S, Gagnol V, Bouzgarrou BC, Ray P. Control of a multi degrees functional redundancies robotic cell for optimization of the machining stability. Procedia CIRP 2017;58:269–74.
[23] Gonul B, Sapmaz OF, Tunc LT. Improved stable conditions in robotic milling by kinematic redundancy. Procedia CIRP 2019;82:485–90.
[24] Celikag H, Sims ND, Ozturk E. Chatter suppression in robotic milling by control of configuration dependent dynamics. Procedia CIRP 2019;82:521–6.
[25] Xiong G, Ding Y, Zhu L. Stiffness-based pose optimization of an industrial robot for five-axis milling. Robot Comput-Integr Manuf 2019;55:19–28.
[26] Schmitz T, Smith KS. Machining Dynamics: Frequency Response to Improved Productivity, Second Edition. New York, NY: Springer; 2019.
[27] Corral J, Pinto C, Campa FJ, Altuzarra O. Surface location error of a parallel robot for routing processes. Int J Adv Manuf Technol 2013;67:1977–86.
[28] Cen L, Melkote SN, Castle J, Appelman H. A wireless force-sensing and model- based approach for enhancement of machining accuracy in robotic milling. IEEE/ ASME Trans Mechatron 2016;21(5):2227–35.
[29] Hou T, Lei Y, Ding Y. Pose optimization in robotic milling based on surface location error. J Manuf Sci Eng 2023;145(8):084501.
[30] Verl A, Valente A, Melkote S, Brecher C, Ozturk E, Tunc LT. Robots in machining. CIRP Ann 2019;68(2):799–822.
[31] Altintas¸ Y, Budak E. Analytical prediction of stability lobes in milling. CIRP Ann 1995;44(1):357–62.
[32] Schmitz TL, Mann BP. Closed-form solutions for surface location error in milling. Int J Mach Tools Manuf 2006;46(12-13):1369–77.
[33] Mohammadi Y, Ahmadi K, September. Structural nonlinearity of robotic machining systems. In: International manufacturing science and engineering conference (Vol. 84263, p. V002T09A009). American Society of Mechanical Engineers; 2020.
[34] Tunc LT, Gonul B. Effect of quasi-static motion on the dynamics and stability of robotic milling. CIRP Annals 2021;70(1):305–8.
[35] Duncan GS, Tummond MF, Schmitz TL. An investigation of the dynamic absorber effect in high-speed machining. Int J Mach Tools Manuf 2005;45(4-5):497–507.